CrystEngComm

Accepted Manuscript

This article can be cited before page numbers have been issued, to do this please use: F. Mokhtari, A. Nehari, Y. Xing, Z. Wang, P. Chen, N. Pruneau, Y. Guyot, C. Comby-Zerbino, X. Xu and K. Lebbou, *CrystEngComm*, 2026, DOI: 10.1039/D6CE00327C.

ROYAL SOCIETY OF CHEMISTRY

rsc.li/crystengcomm

View Article Online
DOI: 10.1039/D6CE00327C

Behind the scenes of sapphire: influence of titanium doping on bubble distribution and propagation in sapphire grown by micro-pulling-down

Faiza MOKHTARI[1], Abdeldjelil NEHARI[1], Yupei XING[1], Zebin WANG[1], Peng CHEN[1], Nicolas PRUNEAU[1,2], Yannick GUYOT[1], Clothilde COMBY-ZERBINO[1], Xiaodong XU[3], Kheirreddine LEBBOU[1]

[1] *Institut Lumière Matière, UMR 5306 Université Lyon1-CNRS, Université de Lyon, Lyon, 69622, Villeurbanne Cedex, France*

[2]*ECM Greentech / Cyberstar Rue de Chamrousse, Voie des Collines 38800 Le Pont-de-Claix – France*

[3]*Jiangsu Key Laboratory of Advanced Laser Materials and Devices, School of Physics and Electronic Engineering, Jiangsu Normal University, Xuzhou 221116, China*

Abstract

Undoped and titanium-doped sapphire (Ti:Al_2O_3) single-crystal rods were grown using the micro-pulling-down (μ-PD) technique to investigate the effect of Ti incorporation on bubble defect formation. Crystals with Ti concentrations of 0, 500, and 1000 ppm were obtained with uniform geometry and good optical quality. Microstructural analysis revealed a strong dependence of bubble distribution and morphology on Ti dopant. Undoped sapphire exhibited only a thin peripheral layer of small spherical bubbles (0–20 μm), whereas Ti-doped crystals showed a significant increase in bubble layer thickness (up to ~370 μm), accompanied by the appearance of elongated and irregular bubble shapes. A quasi-steady-state numerical model, including heat transfer, melt convection, and thermocapillary (Marangoni) effects, was developed to clarify the governing mechanisms. Simulations indicate that increasing Ti concentration enhances the meniscus height and intensifies Marangoni convection, with melt velocities rising from ~5.6 to 20 mm·s^{-1}. The resulting flow structure promotes bubble transport toward the crystal periphery and contributes to their deformation under strong shear near the meniscus. These results provide a consistent interpretation of the relationship between titanium doping, melt flow, and bubble distribution during μ-PD sapphire growth.

Keywords: Sapphire; Micro-pulling-down (μ-PD); Titanium doping; Bubble defects; Marangoni convection

1. Introduction

Sapphire single-crystal (α-Al_2O_3) is a technologically important material due to its exceptional mechanical strength, high melting point (≈2050 °C), excellent chemical stability, and wide optical transparency extending from the ultraviolet to the infrared region. These properties make sapphire widely used in optics, electronics, high-temperature devices, and laser host materials. In particular, sapphire doped with transition metal ions such as titanium has attracted considerable attention because of its outstanding spectroscopic and optical properties [1-3].

Among laser crystals, titanium-doped sapphire (Ti:Al_2O_3) is one of the most important materials for tunable and ultrafast laser systems. The incorporation of Ti^{3+} ions into the corundum lattice gives rise to a very broad emission band ranging approximately from 650 nm to 1100 nm, enabling tunable laser operation and generation of femtosecond pulses [4]. These characteristics have made Ti:sapphire the cornerstone of ultrafast laser technology and an essential component in applications such as high-power amplifiers, lidar transmitters,

View Article Online
DOI: 10.1039/D6CE00327C

spectroscopy systems, and biomedical procedures including ophthalmic surgery. The optical performance of Ti:sapphire for lasers applications strongly depends on the concentration and distribution of Ti^{3+} ions in the crystal lattice as well as the structural perfection of the host crystal [5-7].

Several techniques have been developed for the growth of sapphire and Ti-doped sapphire crystals, including the Czochralski (Cz), Kyropoulos (Ky), Edge-Defined Film-Fed Growth (EFG), and micro-pulling-down (μ-PD) methods [7-10]. The μ-PD technique has attracted increasing attention because it enables the rapid growth of small-diameter rods or fibers with controlled geometry and high growth rates [11]. Moreover, the reduced melt volume in μ-PD growth facilitates detailed experimental investigations and numerical modeling of the thermal and hydrodynamic phenomena occurring during solidification [12].

However, sapphire crystals grown from the melt frequently contain structural defects such as dislocations, inclusions, voids, and gas bubbles that can degrade the optical quality of the material. Bubble defects are particularly problematic because they act as scattering centers, generate optical haze, and reduce laser efficiency [13,14]. These bubbles typically originate from gas entrapment at the solid–liquid interface or from chemical reactions involving residual impurities, crucible materials, or dissolved gases in the melt [15-18]. During crystal growth, bubbles may be transported by buoyancy forces or melt convection and can eventually become trapped at the growth interface, where they are incorporated into the crystal structure [7].

Several studies have investigated bubble formation and propagation in sapphire crystals grown by different techniques. Experimental observations have shown that bubble incorporation depends strongly on growth parameters such as pulling rate, thermal gradients, interface curvature, and melt convection [6]. In the μ-PD process, the complex thermo-fluid dynamics within the melt, including Marangoni convection and forced convection induced by the pulling process, play a key role in determining the trajectories and capture probability of bubbles. In addition, the shape and stability of the crystal–melt interface strongly affect the interaction between bubbles and the growing crystal [19].

Recent investigations combining experimental observations and numerical modeling have significantly improved the understanding of bubble behavior during sapphire growth. Numerical simulations have shown that temperature distribution, melt flow patterns, and electromagnetic heating conditions strongly affect bubble motion and interface interactions [8,19,20]. These multi-scale studies have also demonstrated that bubble characteristics, such as size distribution and spatial arrangement, can evolve during crystal growth due to complex interactions between hydrodynamic forces and solidification dynamics.

Although many studies have focused on the influence of growth parameters on bubble formation, the effect of dopant concentration, particularly titanium, on bubble behavior in sapphire crystals remains insufficiently explored. Titanium incorporation can modify the thermodynamic and kinetic conditions in the melt, influence defect formation mechanisms, and alter the optical absorption properties of the resulting crystal [5,21]. A better understanding of how titanium concentration affects bubble formation and propagation during crystal growth is therefore essential for improving the quality of Ti:sapphire laser materials.

The objective of the present study is to investigate, experimentally and numerically, the influence of titanium concentration on bubble behavior in sapphire rods grown by the μ-PD technique. Sapphire rods with a diameter of 5 mm were grown with different initial titanium

View Article Online
DOI: 10.1039/D6CE00327C

concentrations (0, 500, and 1000 ppm). The rods were subsequently cut into 5 mm-thick wafers and polished for microstructural analysis. Bubble morphology and size distribution were examined using high-resolution optical microscopy in both longitudinal and transverse orientations. To complement the experimental observations, a global finite-element numerical model was developed using the exact geometry of the growth furnace. The model calculates the electromagnetic field, temperature distribution, and melt velocity field, enabling detailed analysis of the thermo-hydrodynamic conditions that govern bubble transport and capture at the growth interface. By combining experimental characterization with numerical modeling, this study aims to provide new insights into the mechanisms controlling bubble behavior in undoped and Ti-doped sapphire crystals grown by the μ-PD method.

2. μ-pd growth of undoped and Ti-doped sapphire rods

Undoped sapphire (Al_2O_3) and titanium-doped sapphire ($Ti:Al_2O_3$) single-crystal rods with Ti concentrations of 500 and 1000 ppm were successfully grown using μ-PD technique. The as-grown crystals exhibited a uniform cylindrical morphology with a diameter of approximately 5 mm. The undoped rod was optically transparent and colorless, whereas the Ti-doped samples displayed a homogeneous light-red coloration, characteristic of Ti^{3+} incorporation within the corundum lattice.

Crystal growth was carried out in a radio-frequency (RF) induction-heated μ-PD furnace (figure 1). The growth assembly consisted of a molybdenum crucible (outer diameter 22 mm, inner diameter 20 mm, height 60 mm) equipped with a capillary die at its base (die diameter 5 mm, orifice diameter 1 mm). An after-heater of similar dimensions surrounded the lower part of the crucible, extending the high-temperature zone below the die and thereby reducing the axial thermal gradient at the solid–liquid interface. This configuration minimized thermally induced stresses and promoted high crystalline quality.

Thermal insulation of the hot zone was ensured by graphite components surrounding the molybdenum crucible and after-heater. Graphite was selected because of its excellent thermal stability at high temperatures and its widespread use in crystal growth furnaces employing molybdenum hot-zone components, providing efficient thermal shielding and reducing heat losses from the growth zone. A transparent quartz tube was positioned below the insulated region, providing a controlled atmosphere and optical access to the growth zone, particularly the region beneath the die where the crystal is pulled. A narrow observation channel was incorporated through the graphite insulation to enable direct visualization of the molten zone, part of the crystal and the die.

The starting charge (~5.2 g) consisted of high-purity (99.999%) Al_2O_3 in the form of crackle and microbeads, including both undoped and Ti-doped compositions. Prior to growth, the chamber was evacuated to approximately 10^{-4} mbar and then backfilled with high-purity argon under continuous flow to prevent oxidation of the molybdenum components. Melting was achieved using an RF induction system operating at 11.2 kHz with a maximum power of 25 kW. Two preliminary melting cycles were performed to stabilize the molten zone and establish a reproducible pendant drop at the die orifice.

Crystal growth was initiated by gently bringing an undoped sapphire seed crystal into contact with the molten drop at the die exit. Due to the steep thermal gradients inherent to the μ-PD process, the approach velocity was carefully controlled to avoid thermal shock. Slight remelting

View Article Online
DOI: 10.1039/D6CE00327C

of the seed tip enabled the formation of a stable liquid meniscus, which is essential for controlled growth. The pulling rate was maintained at 0.5 mm·min^{-1} throughout the process.

The meniscus height and shape, governed by surface tension, growth angle, and the relative position of the solid–liquid interface, were carefully controlled to maintain a constant rod diameter. Stable growth conditions were ensured through precise regulation of the melt temperature and interface position. Real-time monitoring of the meniscus and rod diameter was carried out using a CCD camera through observation windows. Further details of the experimental procedure can be found in previous studies [8,19,22,23].

The resulting sapphire rods exhibited smooth surfaces, uniform diameter, and high optical quality, with no visible macroscopic defects such as cracks demonstrating the reliability of the μ-PD technique for the growth of high-quality undoped and Ti-doped sapphire single crystals (figure 2 a). Wafers of 5 mm in height were then cut from the middle region of each of the three crystal rods, including the Ti:Al_2O_3 crystal, and subsequently well-polished for characterization, ensuring representative sampling despite the known dopant segregation along the growth direction. Figure 2b shows a top and a side view for these wafers.

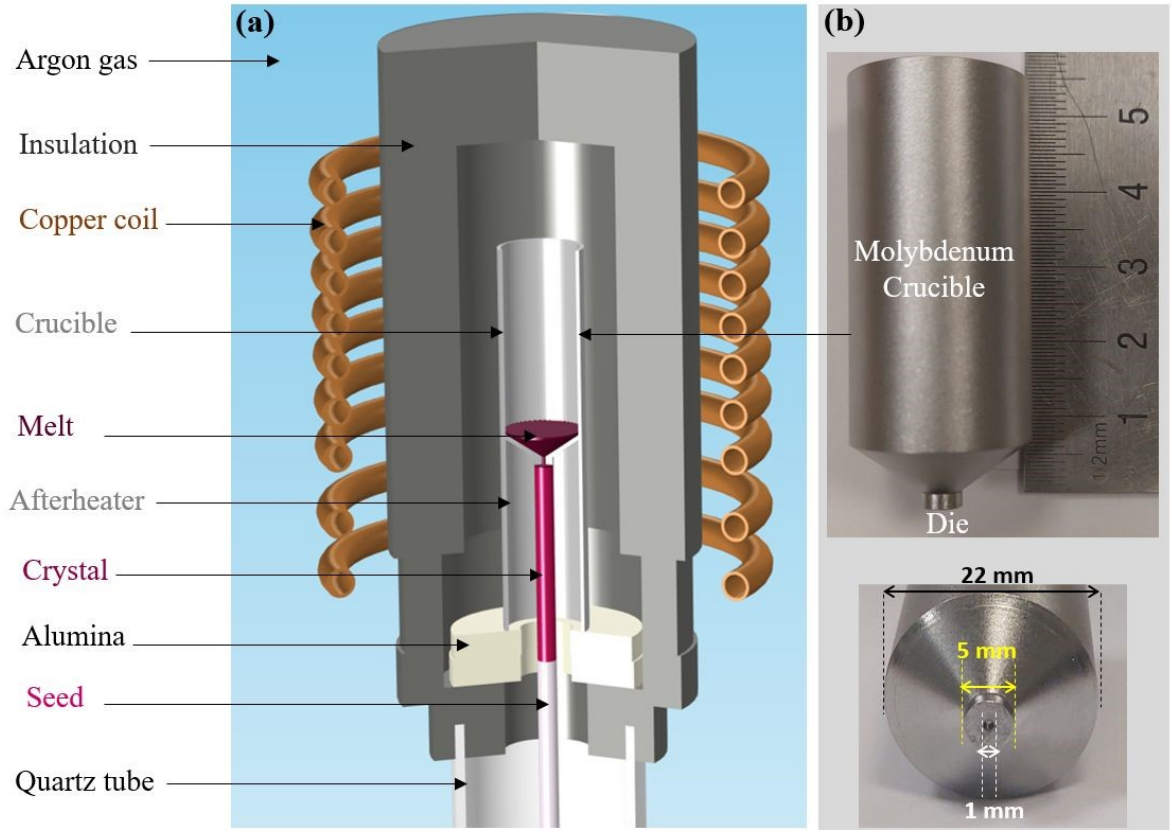

Figure 1. *Schematic of the μ-PD furnace employed for the growth of undoped and titanium-doped sapphire, with the principal components indicated in (a). In (b), photographs of the molybdenum crucible are shown, including front and bottom views, together with the corresponding dimensions of the crucible diameter ($D_{crucible}$ = 22 mm), die diameter (D_{die} = 5 mm), and the orifice through which the melt is withdrawn (D_{hole} = 1 mm).*

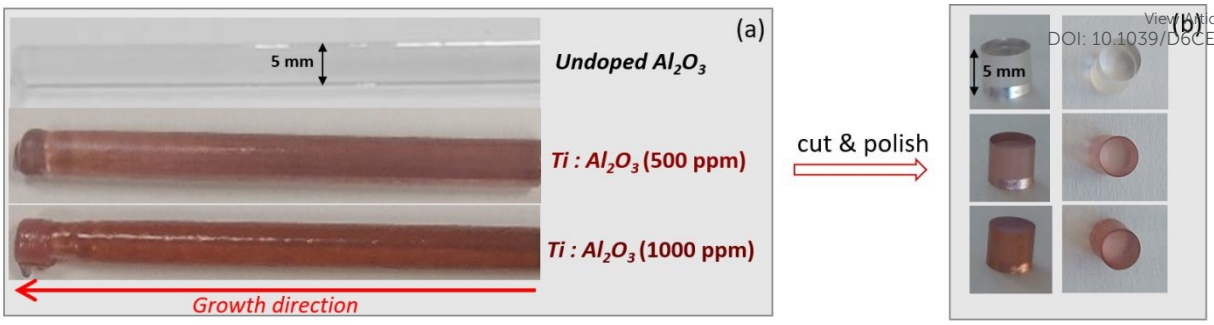

Figure 2. *Undoped and titanium-doped sapphire rods (500 and 1000 ppm Ti, 5 mm diameter) grown using the μ-PD technique. (a) As-grown crystals after solidification. (b) Polished wafers (5 mm thickness) obtained after cutting, showing side view (left) and top view (right).*

3. Microstructural characterization of bubble defects in Al_2O_3 and Ti:Al_2O_3 rods

Gas bubbles in undoped sapphire crystals typically originate from gas entrapment at the solid–liquid interface or from chemical reactions involving residual impurities, crucible materials, raw material and dissolved gases in the melt during heating [15–18]. Such mechanisms are well documented in sapphire growth studies, where gas rejection and interfacial instability lead to bubble incorporation within the crystal lattice. In titanium-doped sapphire, the presence of Ti introduces additional complexity through its interaction with the melt and the evolving crystal. In particular, Ti doping modifies key thermophysical properties such as viscosity, optical absorption coefficient, emissivity and thermal conductivity, which in turn influence bubble nucleation, growth, shape, and spatial distribution.

To investigate bubble distribution, morphology, and size within the sapphire crystals, an optical microscope equipped with transmission and reflection light sources was used, along with various objectives (×50, ×100, ×200, ×500, ×1000, and ×2000). The microscope was coupled to a video camera connected to a computer for image acquisition and processing. Transverse and longitudinal cross sections of the rods were prepared by cutting and subsequent polishing to reduce surface roughness, resulting in surfaces suitable for detailed bubble analysis (figure 2b). Low-magnification images allowed visualization of the overall cross section and the peripheral bubble layers (figure 3), while high-magnification images enabled precise measurement of bubble sizes and detailed observation of bubble shapes (figures 4 and 5). The morphology and size distribution (diameter and length) of bubbles in undoped and Ti-doped sapphire are summarized in Table 1.

The microstructural analysis reveals pronounced differences in bubble formation, size, morphology, and distribution between undoped and titanium-doped sapphire rods (figures 3–5, Table 1). Transverse micrographs show that the cores of all rods are essentially bubble-free. In undoped sapphire (0 ppm Ti), only a few small spherical bubbles are present at the periphery, forming a thin bubble layer of 0–20 μm, with bubble diameter ranging from 4 to 9 μm, and the crystal exhibits a uniform light color. This bubble size in undoped sapphire rods consistent with previous studies [19,23,24] for sapphire rods with 3mm in diameter which was found typically in the range of 2–8 μm.

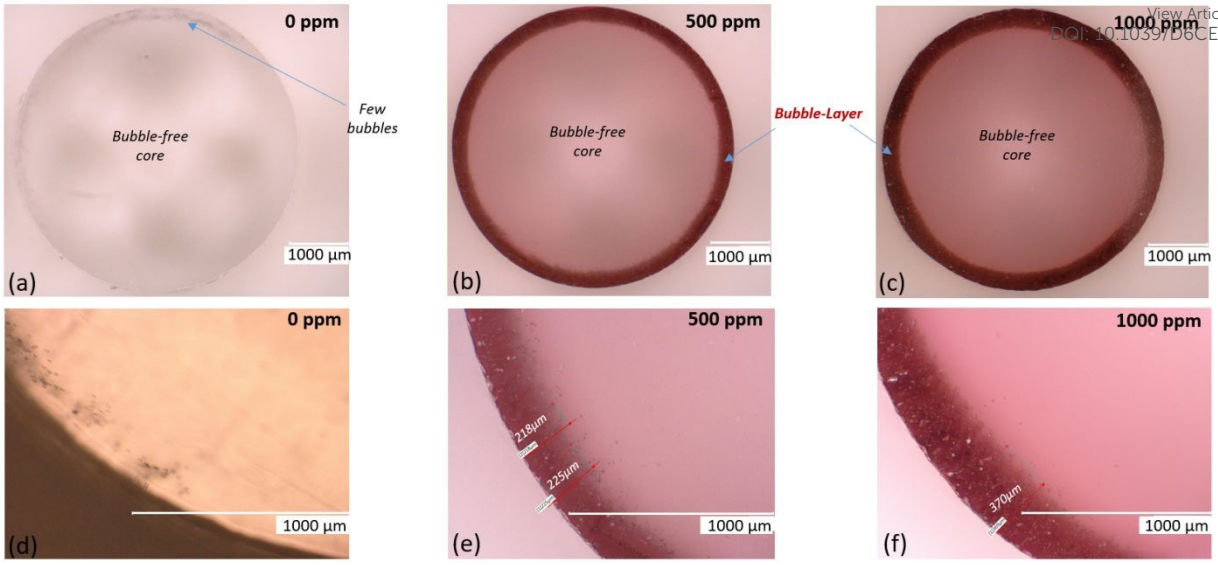

Figure 3. *Transverse optical micrographs of undoped and titanium-doped sapphire wafers cut from rods. Low-magnification images (×50; a–c) show the overall cross-section, while higher magnification (×200; d–f) highlights the bubble layer thickness. The cores of all three rods are essentially bubble-free. At the periphery, only a few isolated bubbles are observed in the undoped sample (a, d). In contrast, titanium-doped rods exhibit a continuous cylindrical bubble layer at the periphery, with thicknesses of approximately 220 µm and 370 µm for 500 ppm (b, e) and 1000 ppm (c, f) Ti concentrations, respectively. Bubble density increases with titanium content, correlating with regions of darker red/brown coloration.*

Titanium doping markedly increases both the thickness and complexity of the peripheral bubble layer. At 500 ppm Ti, the layer expands to 220–240 µm, with bubbles displaying a wide range of shapes, including spherical, elliptical, tailed, elongated, bean, and heart-shaped forms, with spherical bubbles ranging from 4–42 µm and non-spherical bubbles from 10–200 µm (figure 4). These various bubble shapes have also been reported in large Ti:sapphire crystals [8]. At 1000 ppm Ti, the peripheral layer further increases to 310–370 µm, and bubbles reach extreme dimensions, with spherical bubbles of 4–50 µm and non-spherical bubbles extending up to 500 µm, including extremely elongated and highly extended structures (figure 5). High-magnification transverse micrographs (×2000) highlight the diversity of bubble morphologies, reflecting interactions between titanium segregation, melt convection, and local supersaturation. Longitudinal micrographs reveal that, in undoped sapphire, spherical bubbles are arranged along nearly linear features that are generally parallel to the crystal growth direction (figure 5a). Similar bubble-line structures in undoped sapphire rods have previously been reported in the literature [23,24]. In contrast, titanium-doped rods contain elongated bubbles (figure 5b) and, at higher Ti concentrations, excessively long bubbles (figure 5c) with more irregular orientations that are not consistently aligned with the growth direction. This behavior is likely associated with the presence of Ti and its non-uniform distribution within the crystal resulting from segregation during growth. In addition, the peripheral bubble-rich region coincides with a darker red-brown coloration, whereas the core remains lighter in color, suggesting titanium enrichment near the crystal periphery. This segregation may contribute to both the observed color variation and the changes in bubble morphology.

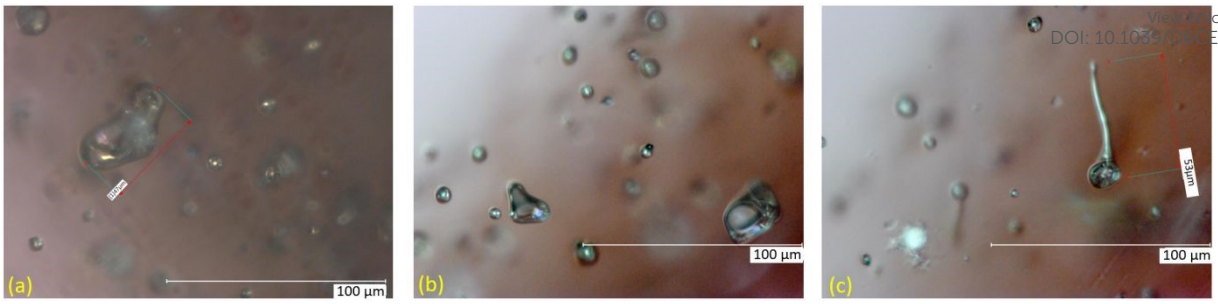

Figure 4. *High-magnification (×2000) transverse micrographs of titanium-doped sapphire rods illustrating the diversity of bubble morphologies. The observed defects include spherical and elliptical bubbles, as well as irregular forms such as bean-shaped, tailed, and heart-shaped structures.*

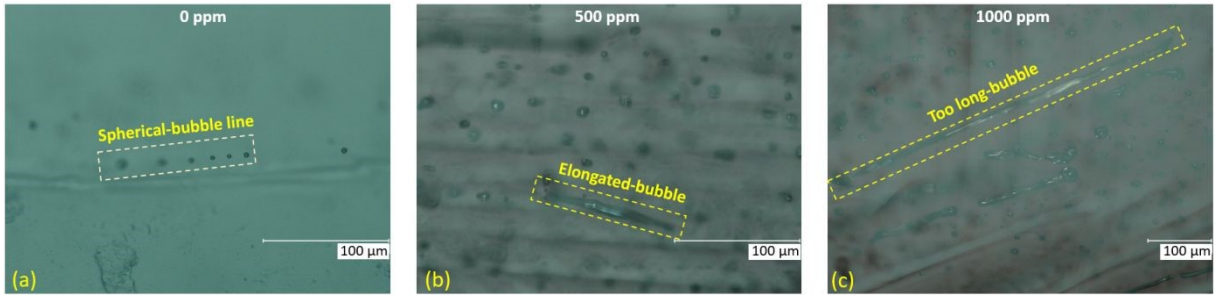

Figure 5. *Longitudinal micrographs of undoped (a) and titanium-doped (b and c) sapphire wafers. Images (a, b) were acquired at ×1000 magnification, and (c) at ×500 to capture the full length of elongated bubbles. In the undoped sapphire, spherical bubbles are observed to align along linear features, whereas titanium-doped rods exhibit elongated and extensively long bubbles. The reduced magnification in (c) highlights the total length of an exceptionally long bubble.*

Table 1. Morphology and size distribution of bubble defects in undoped and Ti-doped sapphire rods

Ti concentration (ppm)	Peripheral bubble layer thickness (µm)	Dominant bubble morphologies	Spherical bubble diameter (µm)	Non-spherical bubble size range (µm)
0	0–20	Spherical	4–9	—
500	220–240	Spherical; elliptical; elongated; tailed; irregular (bean-/heart-shaped)	4–42	10–200
1000	310–370	Spherical; elongated; highly elongated; irregular (bean-/heart-shaped)	4–50	10–500

4. Numerical Analysis of Thermocapillary Flow and Bubble Dynamics in μ-PD Sapphire Growth

Building on the preceding discussion of crystal growth dynamics and bubble formation, numerical simulations of sapphire growth by the μ-PD method were performed to investigate the interactions among melt flow, meniscus shape, and bubble behavior. A quasi-steady-state (QSS) global finite-element model was employed, accounting for heat conduction in solid components, natural convection in the melt and surrounding argon atmosphere, thermocapillary (Marangoni) flow along the melt free surface and meniscus, and radiative heat transfer within semitransparent media (melt, crystal, and quartz tube) as well as across argon-filled gaps. The simulated furnace geometry reproduced the experimental setup, with key parameters such as rod diameter, seed dimensions, and meniscus height matching the measured values.

The computational geometry was constructed using the exact dimensions of all furnace components (Fig. 1). The measured rod diameter (Fig. 2) and meniscus height (Fig. 6, left) were also incorporated into the model. Assuming axisymmetric and quasi-steady-state conditions, the governing equations are given below.

In the solid parts of the furnace:

$$-\nabla(\mathrm{k}\nabla\mathrm{T}) = \mathrm{Q} \tag{1}$$

In the melt:

$$\nabla.(\rho \boldsymbol{V}) = 0 \tag{2}$$

$$(\boldsymbol{V}.\nabla)\rho\boldsymbol{V} = -\nabla p + \mu\nabla.(\rho\nabla\boldsymbol{V}) + \rho\,\boldsymbol{g}(1-\beta(T-T_m)) \tag{3}$$

$$\nabla.(\rho c_P \boldsymbol{V}T) + \nabla.(-k\nabla T) + a_m(4\pi I_b - G) = 0 \tag{4}$$

In the crystal:

$$\nabla.(-k\nabla T) + a_c(4\pi I_b - G) = 0 \tag{5}$$

where T is the temperature, $\boldsymbol{V}$ is the velocity vector p is the pressure, $\boldsymbol{g}$ is the gravitational acceleration, T_m is the melting temperature, and Q is the volumetric heat source associated with Joule heating. The source term Q is applied only in electrically conductive regions (crucible and after heater), while it is set to zero in non-conductive materials. The parameters ρ, μ, c_P, k and β denote the density, dynamic viscosity, specific heat, thermal conductivity, and thermal expansion coefficient, respectively; a_m and a_c are the absorption coefficients of the melt and crystal; I_b the blackbody intensity, and G the incident radiative flux.

Additional details regarding the mathematical formulation and numerical implementation are available in our previous work [19]. Furthermore, the computational domain was discretized using an unstructured mesh with strong local refinement near the melt–solid (solidification front) and melt–gas (meniscus) interfaces, where steep gradients of temperature, velocity, and electromagnetic forces occur. The minimum element size in these regions was approximately 0.002 mm. A mesh independence study was performed using progressively refined grids up to 1.5×10^6 elements, and variations in key monitored quantities (maximum temperature and peak velocity) between the two finest meshes were below 5 %. The coupled governing equations were solved iteratively until the normalized residuals for governing equations decreased below 10^{-5}. Validation of the numerical model is provided in our previous papers [19, 22]. Table 2

View Article Online
DOI: 10.1039/D6CE00327C

summarizes the thermophysical properties for sapphire melt and crystal, molybdenum crucible and afterheater, graphite insulation, copper coil and argon gas used for computations. Using the ideal gas law at atmospheric pressure, the density of argon is approximated by the temperature-dependent relation $\rho_{gas} = 489/T$, where ρ is in $g.m^{-3}$ and T is the temperature in Kelvin [25]. The absorption coefficient of sapphire increases with higher titanium (Ti) doping concentrations. Values for undoped and doped sapphire are 19 m^{-1} and 100 m^{-1} as shown in Table 2.

Table 2 Thermophysical properties used in simulation.

Property	System	Phase	Value / Function of temperature T(K)	References
Density ρ (g.cm⁻³)	Al_2O_3	S	3.96	[19, 26]
	Al_2O_3	L	3.00	[19, 26, 27]
	Insulation	S	1.2	[28]
	Copper	S	8.96	[29]
	Molybdenum	S	10.28	[30]
	Quartz	S	2.65	[30]
	Argon	G	489×10^{-6}/ T	[25]
Melting point T□ (K)	Al_2O_3	—	2323	[26]
Dynamic viscosity μ (Pa·s)	Al_2O_3	L	0.058	[26, 27]
	Argon	G	10^{-6} exp[-3.36 + 0.73 ln(T) - 1.37 × 10^{-3} $(\ln(T))^2$ + 1.30 × 10^{-5} $(\ln(T))^3$ - 4.6 × 10^{-8} $(\ln(T))^4$]	[28]
Emissivity ε	Al_2O_3	S	0.9	[26, 27, 32]
	Al_2O_3	L	0.33	[26, 27, 33]
	Insulation	S	0.9	[29, 31]
	Quartz	S	0.85	[31]
	Copper	S	0.2	[29]
	Molybdenum	S	0.2	[31, 34]
Absorption coefficient a (m^{-1})	Al_2O_3	S	19.2	[26, 27, 35-37]
	$Ti:Al_2O_3$	S	100	
Thermal expansion coefficient β (K^{-1})	Al_2O_3	L	1.8×10^{-5}	[20, 29,38]
Electrical conductivity σ (S.m⁻¹)	Copper	S	5.81×10^{7}	[28]
	Molybdenum	S	1.97×10^{7}	[20, 30]
Thermal conductivity k (W/m·K)	Al_2O_3	L	3.5	[19, 20, 26]
	Al_2O_3	S	5	[27, 33]
	Argon	G	$0.01 + 2.5 \times 10^{-5}$ T	[31]
	Molybdenum	S	10	[31]
Heat capacity cp (J/kg·K)	Al_2O_3	L	767	[19, 20, 26]
	Quartz	S	74	[31]
	Molybdenum	S	10	[31]
	Argon	G	521	[31]
Temperature surface tension gradient dσ/dT (N/m·K)	Al_2O_3	L	-3.5×10^{-4}	[19,20,38] [19, 20, 26, 27]

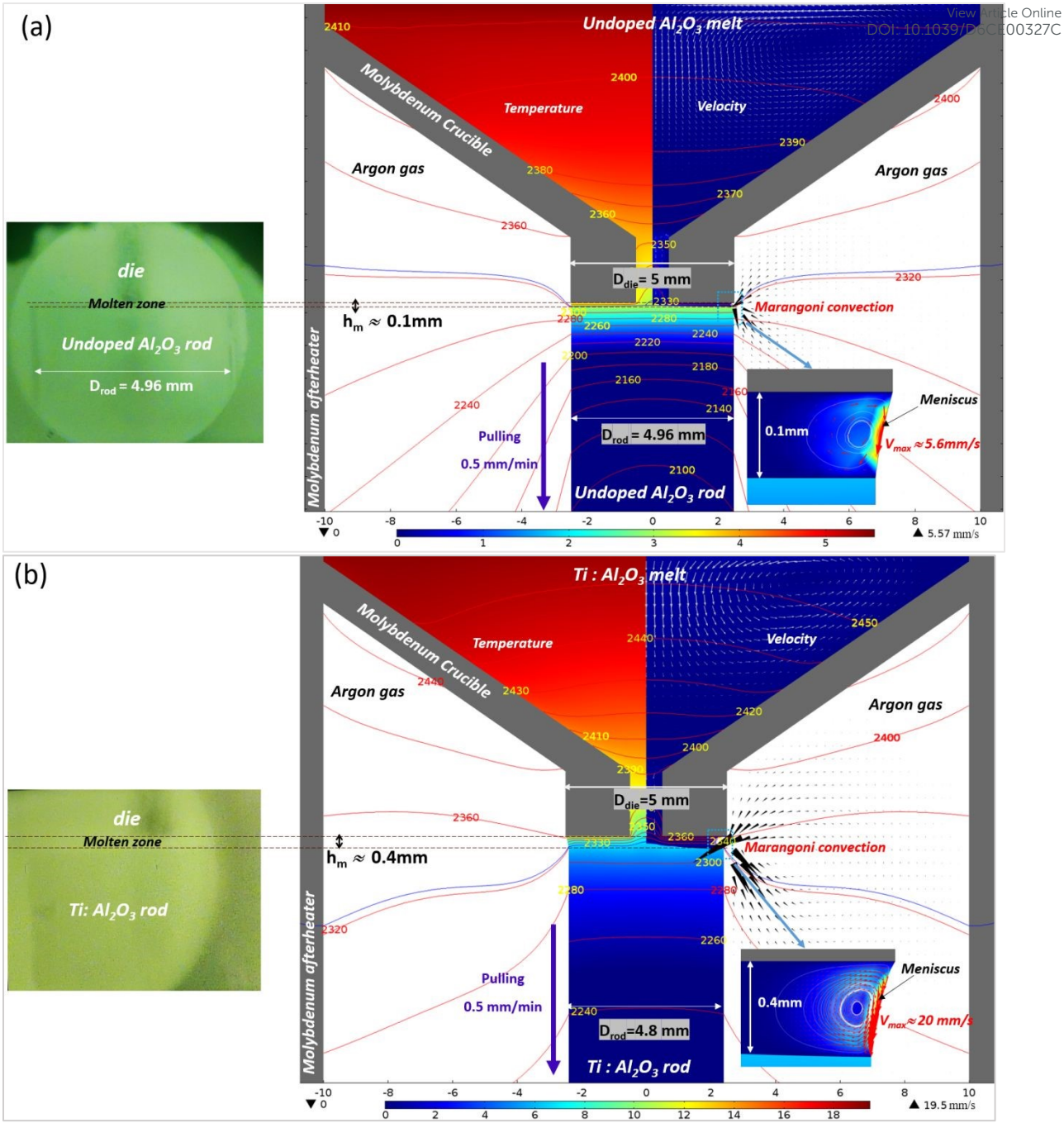

Figure 6. *Comparison between (a) undoped sapphire and (b) titanium-doped sapphire (1000 ppm) during μ-PD crystal growth. Left: Photographs captured through the furnace observation window, showing the bottom of the die (D_{die} = 5 mm), the molten zone, the meniscus, and the most recently grown crystal. The meniscus height is approximately h□ ≈ 0.1 mm for (a) and ≈ 0.4 mm for (b). The crystal diameter is D_{rod} ≈ 4.96 mm for (a) and ≈ 4.8 mm for (b), at a pulling rate of 0.5 mm·min⁻¹. Right: Simulated temperature and velocity fields in the melt, crystal, and surrounding atmosphere. Red lines represent isotherms, with the blue line indicating the melting temperature (T_m = 2323 K). Black arrows denote gas velocity vectors near the meniscus, while white arrows indicate velocity vectors in the melt; their magnitudes are given by the color bar (in the bottom of each case). Insets at the bottom of each case provide a zoomed view of the flow field near the meniscus (red velocity vectors). Red arrows indicate velocity vectors in the molten zone. Strong Marangoni convection near the meniscus is identified as a primary mechanism driving bubble formation and entrapment at the crystal periphery, particularly in the titanium-doped case.*

View Article Online
DOI: 10.1039/D6CE00327C

The computed temperature field exhibits strong spatial non-uniformities as shown in figure 6, with peak temperatures near the molybdenum crucible wall at the mid-height plane of the induction coil [22] and a gradual decrease toward the furnace boundaries, where the argon temperature approaches ambient conditions. These temperature gradients naturally generate surface tension variations along the melt surface, inducing thermocapillary convection that dominates transport within the molten zone under μ-PD conditions, as buoyancy effects remain negligible due to the small system size and stable thermal stratification [19]. The intensity of this flow, quantified by the Marangoni number $Ma = \left|\frac{\partial\gamma}{\partial T}\right|\frac{h_m \Delta T}{\mu\alpha}$, where h_m the meniscus length, ΔT the temperature difference along the meniscus, and μ and α are the dynamic viscosity and thermal diffusivity of the melt, respectively [11,19,20,22].

Numerical results (figure 6) indicate that increasing the meniscus height from 0.1 mm in undoped Al_2O_3 to 0.4 mm in Ti:Al_2O_3 leads to a marked rise in the Marangoni number from 40 to 160, accompanied by an increase in melt velocity from 5.6 to 20 mm·s^{-1} and a transition in meniscus shape from slightly convex to highly convex. This amplified thermocapillary flow directly influences bubble formation and transport: in undoped sapphire, the experimentally observed small meniscus height (~0.1 mm) produces a weak Marangoni vortex with very low intensity (5 mm·s^{-1}), resulting in a thin peripheral bubble layer of only 0–20 μm. Most of the molten zone remains dominated by heat diffusion, with melt particles moving primarily in the horizontal direction, limiting bubble transport and peripheral accumulation. In contrast, in Ti-doped sapphire with 1000 ppm Ti and a meniscus height of ~0.4 mm, the Marangoni-induced vortex is significantly larger, approximately matching the meniscus height and the experimentally observed thickness of the bubble-rich layer (~0.4 mm), as shown in the insets of figure 6. In this region, the melt exhibits a vertically downward velocity close to the meniscus, which facilitates the transport of bubbles from the molten zone to the periphery of the crystal. This mechanism accounts for the substantially thicker peripheral bubble layer (220–370 μm) populated by bubbles of varied sizes and complex morphologies, including spherical, elongated, tailed, and irregular forms, while the core remains largely bubble-free. Together, these results demonstrate a direct correlation between meniscus height, Marangoni-induced vortex size, and the thickness and morphology of the peripheral bubble layer, confirming that thermocapillary convection is the key factor controlling bubble distribution, growth, and deformation during sapphire μ-PD crystallization.

Moreover, in the case of Titanium doped sapphire at the meniscus line, flow intensity is stronger (about 20mm/s) than in the case of undoped sapphire (about 5.4 mm/s) and velocity vectors are mainly directed downward. This can be directly related to the elongated and very long bubbles observed at the crystal outer surface in figure 5b and 5c.

It should be emphasized that, at the relatively low pulling rate used in this study (0.5 mm·min^{-1}), the forced convection generated in the melt core remains weak, with velocities below 0.2 mm·s^{-1} for both undoped and Ti-doped sapphire. These values are significantly lower than those predicted near the meniscus, where Marangoni-driven velocities reach 5.6 mm·s^{-1} and 20 mm·s^{-1}, respectively. Consequently, bubble transport is controlled predominantly by thermocapillary convection in the meniscus region, leading to preferential bubble accumulation at the crystal periphery, while the crystal core remains largely bubble-free. This prediction is in excellent agreement with the experimental observations presented in the previous section, which revealed the formation of a peripheral bubble-rich layer and the absence of significant bubble incorporation in the crystal core.

View Article Online
DOI: 10.1039/D6CE00327C

Table 3 Comparison of Al_2O_3 and Ti:Al_2O_3 growth characteristics.

Parameter	Al_2O_3	Ti:Al_2O_3
Pulling rate	0.5mm/min	0.5mm/min
Crystal diameter (mm)	4.96	4.8
Meniscus height (mm)	0.1	0.4
Meniscus shape	slightly convex	highly convex
Molten zone velocity (mm.s^{-1})	5.6	20
Marangoni number	40	160

Furthermore, the difference in absorption coefficients between undoped and titanium-doped crystals (19 m^{-1} vs. 100 m^{-1}) significantly enhances the thermal gradients at the crystal–melt interface, particularly in the vicinity of the meniscus. This effect can be attributed to the intensification of Marangoni-driven convection. As illustrated in Fig. 7, the temperature gradient in this region ranges from 70 to 80 K·mm^{-1} for the undoped crystal, while it increases to 105–120 K·mm^{-1} in the doped case.

In the initial portion of the crystal–melt interface, the temperature gradient remains nearly uniform for both compositions. This observation is consistent with the absence of bubbles in the crystal core, suggesting a relatively stable thermal and hydrodynamic environment in this region. Such stability is typically associated with limited convective perturbations and a well-controlled solidification front. The magnitude of the temperature gradients obtained in this study is in good agreement with values reported in the literature. For instance, gradients on the order of ~100 K·mm^{-1} have been reported for sapphire/YAG eutectic fibers [11], while a broader range between 60 and 120 K·mm^{-1} has been found for sapphire rods [20] depending on parameters such as thermal insulation thickness.

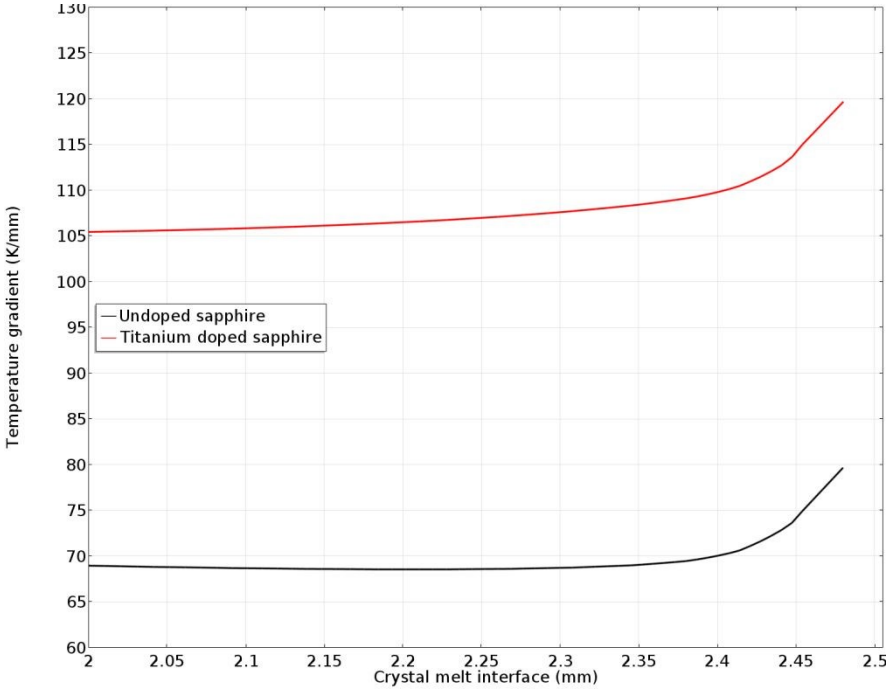

Figure 7. *Comparison between temperature gradient at the melt-crystal interface for undoped sapphire and titanium-doped sapphire (1000 ppm) in black and red colors respectively.*

View Article Online
DOI: 10.1039/D6CE00327C

5. Conclusion

This study demonstrates that titanium doping strongly modifies bubble formation during μ-PD growth of sapphire by altering melt hydrodynamics. While undoped sapphire exhibits only a thin peripheral layer of small spherical bubbles, Ti-doped crystals show a substantial increase in bubble layer thickness, accompanied by the formation of elongated and highly irregular bubble morphologies as the Ti concentration increases.

Numerical results reveal that this behavior is governed by thermocapillary (Marangoni) convection. The increase in Ti content leads to a higher meniscus height and a significant rise in Marangoni flow intensity, generating a strong vortex localized near the meniscus. This flow structure promotes downward flow along the free surface and drives bubbles toward the crystal periphery. The good agreement between the calculated vortex size and the experimentally observed thickness of the bubble-rich layer confirms that bubble distribution is primarily controlled by Marangoni-driven convection.

In addition, the increase in flow intensity and velocity gradients near the meniscus, as revealed by numerical simulations, explains the progressive transition from small, spherical to larger, elongated bubbles, through shear-induced deformation, while the experimental observation of a nearly bubble-free rod core combined with these numerical results, demonstrates that this incorporation mechanism remains confined to the peripheral regions close to the meniscus.

These results establish that bubble incorporation in μ-PD sapphire is mainly governed by the coupling between meniscus geometry and thermocapillary flow, both of which are strongly influenced by titanium doping.

Acknowledgements

This work was conducted within the framework of Idemo program (SEPO450) and FEDER (SaphirTEC) projects. The authors would like to thank the Auvergne Rhone Alpe region for their help and support. We also thank CNRS (ScintLab), the ANR, Labcom program (SaphirLab) and China Scholarship Council (CSC) for their support and assistance.

References

1. Tatartchenko VA. Sapphire crystal growth and applications. In: Capper P, editor. *Bulk crystal growth of electronic, optical and optoelectronic materials*. London: John Wiley & Sons; 2005. p. 300–334. https://doi.org/10.1002/9780470012086.ch10
2. Moulton PF. Spectroscopic and laser characteristics of Ti:Al_2O_3. *J Opt Soc Am B*. 1986;3(1):125–133. https://doi.org/10.1364/JOSAB.3.000125
3. Boulon G. Fifty years of advances in solid-state laser materials. *Opt Mater*. 2012;34(3):499–512. https://doi.org/10.1016/j.optmat.2011.04.018
4. McKinnie IT, Oien AL, Warrington DM, Tonga PN, Gloster LAW, King TA. Ti^{3+} ion concentration and Ti:sapphire laser performance. *IEEE J Quantum Electron*. 1997;33(7):1221–1230. https://doi.org/10.1109/3.594888
5. Nehari A, Duffar T, Ghezal EA, Lebbou K. Chemical segregation of titanium in sapphire single crystals grown by micro-pulling-down technique: Analytical model and experiments. *Cryst Growth Des*. 2014;14(12):6492–6496. https://doi.org/10.1021/cg5013582

6. Li H, Ghezal EA, Alombert-Goget G, Breton G, Ingargiola JM, Brenier A, Lebbou K. Qualitative and quantitative bubble defects analysis in undoped and Ti-doped sapphire crystals grown by Czochralski technique. *Opt Mater*. 2014;37:132–138. https://doi.org/10.1016/j.optmat.2014.05.012
7. Ghezal EA, Li H, Nehari A, Alombert-Goget G, Brenier A, Lebbou K, Joubert MF, Soltani MT. Effect of pulling rate on bubble distribution in sapphire crystals grown by the micro-pulling-down (μ-PD) technique. *Cryst Growth Des*. 2012;12(8):4098–4103. https://doi.org/10.1021/cg300589h
8. Pruneau N, Mokhtari F, Jandot R, Nouri A, Boucheikha O, Nehari A, Lebbou K. Bubble behavior in titanium-doped sapphire crystals: From micro to macro scale. *CrystEngComm*. 2026. https://doi.org/10.1039/D5CE01214G
9. Zermout S, Mokhtari F, Nehari A, Lasloudji I. Numerical study on the effect of additional resistive heating and crystal rotation on sapphire single crystals grown by the Kyropoulos method. *CrystEngComm*. 2018;20(35):5220–5227. https://doi.org/10.1039/C8CE00972D
10. Zermout S, Mokhtari F, Nehari A, Lasloudji I, Haddad F, Merah A. 3D anisotropic stress analysis during Kyropoulos growth of sapphire single crystal. *Cryst Res Technol*. 2019;54(8):1900058. https://doi.org/10.1002/crat.201900058
11. Rudolph P, Yoshikawa K, Fukuda T. Studies on meniscus and diameter stability during the growth of fiber crystals by the micro-pulling-down method. *Jpn J Appl Phys*. 2000;39(10):5966–5969. https://doi.org/10.1143/JJAP.39.5966
12. Fukuda T, Rudolph P, Uda S. *Fiber crystal growth from the melt*. Berlin: Springer; 2004.
13. Zhang L, Zuo H, Zhou J, Sun J, Xing D, Han J. Haze in sapphire crystals grown by SAPMAC method. *Cryst Res Technol*. 2011;46(7):669–675. https://doi.org/10.1002/crat.201100122
14. Borodin A, Steriopolo TA, Tatarchenko VO, Yalovets TN. Control over gas bubble distribution in shaped sapphire crystals. *Cryst Res Technol*. 1985;20(3):301–306. https://doi.org/10.1002/crat.2170200303
15. Vyshnevskiy SV, Kryvonosov YV, Lytvynov LA. Foreign phase inclusions in Ti:sapphire grown in a carbon-containing medium. *Funct Mater*. 2006;13(2):239–243.
16. Bunoiu OM, Duffar T, Nicoara I. Gas bubbles in shaped sapphire. *Prog Cryst Growth Charact Mater*. 2010;56(3–4):123–145. https://doi.org/10.1016/j.pcrysgrow.2010.09.001
17. Vorob'ev A, Kalaev V, Mazaev K. Chemical model of sapphire crystal growth by Kyropoulos technique. *J Cryst Growth*. 2023;612:127196. https://doi.org/10.1016/j.jcrysgro.2023.127196
18. Wang GG, Zhang MF, Zhang HB, He XD, He JC. Study on inclusions in large sapphire optical crystal grown by SAPMAC method. *Chin J Aeronaut*. 2006;19(4):355–360. https://www.researchgate.net/publication/266408209_Study_on_Inclusions_in_Large_Sapphire_Optical_Crystal_Grown_by_SAPMAC_Method
19. Mokhtari F, Wollesen L, Nehari A, Lebbou K. Experimental and numerical analysis on bubble behavior in sapphire rods grown by micro-pulling-down. *Mater Res Bull*. 2025;197:113933. https://doi.org/10.1016/j.materresbull.2025.113933
20. Fang HS, Yan ZW, Bourret-Courchesne ED. Numerical study of the micro-pulling-down process for sapphire fiber crystal growth. *Cryst Growth Des*. 2011;11(1):121–129. https://doi.org/10.1021/cg101021t

21. Xuan L, Duffar T. The growth of titanium-doped sapphire for laser applications. *Prog Cryst Growth Charact Mater*. 2025;71(2):100666. https://doi.org/10.1016/j.pcrysgrow.2025.100666
22. Chen P, Mokhtari F, Guyot Y, Nehari A, Pillonnet A, Xu X, Lebbou K. Ce^{3+} doped Al_2O_3–YAG binary and Al_2O_3–YAG–ZrO_2 ternary eutectic ceramics solidified by micro-pulling-down technique: Numerical analysis, microstructure and optical characterization. *Opt Mater*. 2026. https://doi.org/10.1016/j.optmat.2026.117941
23. Bouaita R, Alombert-Goget G, Ghezal EA, Nehari A, Benamara O, Benchiheub M, Cagnoli G, Yamamoto K, Xu X, Motto-Ros V, Li H, Dujardin C, Lebbou K. Seed orientation and pulling rate effects on bubbles and strain in sapphire grown by μ-PD. *CrystEngComm*. 2019;21(27):4200–4211. https://doi.org/10.1039/C9CE00510B
24. Ghezal EA, Nehari A, Lebbou K, Duffar T. Observation of gas bubble incorporation during micro-pulling-down growth of sapphire. *Cryst Growth Des*. 2012;12(11):5715–5719. https://doi.org/10.1021/cg301232r
25. Tsien H. Thermodynamic properties of gas at high temperatures and pressures. *Jet Propul*. 1955;25(9):478–480.
26. Wu M, Liu L, Ma W. Control of melt–crystal interface shape during sapphire crystal growth by heat exchanger method. *J Cryst Growth*. 2017;474:31–36. https://doi.org/10.1016/j.jcrysgro.2016.12.047
27. Samanta G, Yeckel A, Daggolu P, Fang H, Bourret-Courchesne ED, Derby JJ. Analysis of limits for sapphire growth in a micro-pulling-down system. *J Cryst Growth*. 2011;335(1):148–159. https://doi.org/10.1016/j.jcrysgro.2011.09.015
28. Vogel E. Reference viscosity of argon at low density in the temperature range from 290 K to 680 K. *Int J Thermophys*. 2010;31(3):447–461. https://doi.org/10.1007/s10765-010-0760-6
29. Müller G, Métois JJ, Rudolph P. *Crystal growth: From fundamentals to technology*. Amsterdam: Elsevier; 2004.
30. Draa A, Mokhtari F, Lasloudji I, Zermout S, Lebbou K. Internal radiation effect on semiconductor β-Ga_2O_3 crystals grown by the VB method and anisotropic thermal stress. *J Cryst Growth*. 2024;648:127910. https://doi.org/10.1016/j.jcrysgro.2024.127910
31. Yan D, Guo Z, Chen X, Li K, Zhao J, Hu W. Rapid prediction of interface morphology and oxygen transportation in crystal growth based on the response surface method. *J Cryst Growth*. 2025;649:127935. https://doi.org/10.1016/j.jcrysgro.2024.127935
32. Demina SE, Bystrova EN, Postolov VS, Eskov EV, Nikolenko MV, Marshanin DA, Kalaev VV. Use of numerical simulation for growing high-quality sapphire crystals by the Kyropoulos method. *J Cryst Growth*. 2008;310(7–9):1443–1447. https://doi.org/10.1016/j.jcrysgro.2007.11.083
33. Nguyen TP, Chuang HT, Chen JC, Hu C. Effect of power history on the shape and thermal stress of a large sapphire crystal during the Kyropoulos process. *J Cryst Growth*. 2018;484:43–49. https://doi.org/10.1016/j.jcrysgro.2017.12.027
34. Demina SE, Bystrova EN, Lukanina MA, Mamedov VM, Yuferev VS, Eskov EV, Nikolenko MV, Postolov VS, Kalaev VV. Numerical analysis of sapphire crystal growth by the Kyropoulos technique. *Opt Mater*. 2007;30(1):62–65. https://doi.org/10.1016/j.optmat.2006.11.012
35. Ma W, Zhao L, Ding G, Yang Y, Lv T, Wu M, Liu L. Numerical study of heat transfer during sapphire crystal growth by heat exchanger method. *Int J Heat Mass Transf*. 2014;72:452–460. https://doi.org/10.1016/j.ijheatmasstransfer.2014.01.033

36. Liu W, Lu J, Chen H, Yan W, Min C, Lian Q, Xu Y. Study on crystal–melt interface shape of sapphire crystal growth by the KY method. *J Cryst Growth*. 2015;431:15–23. https://doi.org/10.1016/j.jcrysgro.2015.08.018
37. Tsiapkinis I, Wintzer A, Dadzis K. Validation of 3D and 2D thermal and electromagnetic models for high-frequency induction heating in crystal growth processes. *J Cryst Growth*. 2024;643:127800. https://doi.org/10.1016/j.jcrysgro.2024.127800
38. Mokhtari F, Chen P, Nehari A, Guyot Y, Xu X, Lebbou K. Experimental and numerical study on Al_2O_3–YAG binary and Al_2O_3–YAG–ZrO_2 ternary eutectic ceramic rods at different μ-PD growth stages. *J Alloys Compd*. 2026;**in press**. https://doi.org/10.1016/j.jallcom.2026.188169

View Article Online
DOI: 10.1039/D6CE00327C

Data Availability Statement

TITLE: Behind the scenes of sapphire: the influence of titanium doping on bubble distribution in sapphire obtained by micro pulling down and how titanium guides the bubble propagation

All data generated or analyzed during this study are included in the manuscript. The datasets are fully presented within the figures and tables. No additional datasets were deposited in public repositories.

Prof. Faiza MOKHTARI

Institut Lumière Matière

UCBL

France